# Metallic photonic-band-gap filament architectures for optimized incandescent lighting

Sajeev John and Rongzhou Wang

*Department of Physics, University of Toronto, 60 St. George Street, Toronto, Ontario, Canada M5S 1A7*

We identify an optimized three-dimensional metallic photonic-band-gap filament architecture for electrically pumped, quasithermal, visible light emission. This identification is based on extensive band structure and finite-difference time-domain calculations of metallic photonic crystals. The optimum structure consists of an inverse square-spiral photonic crystal, exhibiting a large bandwidth optical passband below the effective plasma screening frequency of the periodically structured metal. Light emission from the interior surfaces of the filament to the interior air channels occurs exclusively into the passband modes, enabling high-efficiency conversion of electrical energy into visible light.

PACS number(s): 42.70.Qs, 44.40.+a

## I. INTRODUCTION

Blackbody radiation [1] is a fundamental property of matter at finite temperatures. Early experiments of Kirchhoff [2] verified that the Planck distribution of emitted photons is a consequence of establishing thermodynamic equilibrium between the light emitters and their resulting radiation field (for a review see Ref. [3]). In the absence of such an equilibrium, deviations from the Planck distribution may occur [3,4]. Traditionally incandescent lighting filaments, despite being driven from equilibrium exhibit characteristic features of the Planck distribution. At a temperature below their melting point, electrical and thermal energy is primarily converted to unwanted infrared radiation rather than visible light. A striking set of recent experiments [5] has revealed that certain microstructured tungsten filaments, driven out of thermal equilibrium by electrical pumping, can exhibit significant deviations from the blackbody spectrum. This suggests the possibility of higher efficiency incandescent lighting, through suitable filament microstructure.

In this paper we propose an architecture for metallic photonic-band-gap (PBG) [6,7] filaments consisting of a three-dimensional lattice of spiral posts [8] that significantly improves and optimizes the emission of light, resulting from electrical pumping, into a desired band of frequencies. We present photonic band structure and finite-difference time-domain (FDTD) calculations of the electromagnetic mode spectrum and light emission characteristics of a wide variety of metallic photonic crystals. Our numerical search reveals that the optimum filament describes an inverse diamond:3 PBG structure [8] in which spiral arms of air, in an iridium background, connect the third nearest neighbor points of a diamond lattice. This structure is unique in having a high bulk plasma frequency, a high melting point, and an isolated, large-bandwidth, optical passband below the continuum of allowed bands. This passband consists of optical modes that propagate through a connected air network within the filament and arises from a periodic array of hollow "metallic boxes" that are optically connected. This inverse spiral structure is a more functional design than a recently studied tungsten inverse opal structure [9] and a more ideal structure for light emission than the tungsten woodpile [10]. Besides, the square spirals can be easily fabricated by the glancing angle

deposition method [11,12] or the direct laser writing method [13].

Recently, Lin *et al.* heated a three-dimensional (3D) tungsten woodpile with a plasma cutoff wavelength of 2.5 $\mu$m up to 1500 K [5]. By electrically pumping the metallic backbone, a sharp radiation peak was observed at $\lambda \sim 1.8$ $\mu$m at 1535 K, that, unlike standard blackbody radiation, remains fixed over a range of temperature. Even more controversial [14,15] is the observation that under strong pumping, this peak may exceed the radiation intensity of an ideal blackbody.

In order to reconcile these striking experimental observations, it is important to consider the role of nonequilibrium effects. Although a temperature may be associated with vibrations of the metallic lattice atoms as they are heated by passing electrical current, the electronic degrees of freedom of the filament may not be in thermodynamic equilibrium. Given the large amount of interior surface area in a metallic PBG filament, a significant contribution to electrical resistance in the metal may arise from scattering of electrons from these interior surfaces. When such metal surfaces are rough, have sharp edges, or host small metal particles (created by the fabrication process) localized surface plasmon resonances may arise [16]. These plasmonic resonators may be excited through electronic collisions with the interior surfaces and they may then emit light into the optical passband of the PBG filament. Recently, we have demonstrated [17] that, for strong plasmonic resonances [18], nonlinear Bloch waves [19], with laserlike input-output characteristics can be excited within the optical passband of a structured metal.

In earlier work [17], we considered a simplified two-dimensional (2D) model of a metallic filament with a band structure for only E-polarized (electric field normal to the plane of periodicity) light. In the present paper, we describe the realistic band structure for a 3D PBG filament with an optical passband in which electric field vectors can be both parallel and perpendicular (H polarization) to the interior metal surfaces. These H-polarization components are crucial for exciting localized surface plasmon resonances that, in turn, emit light through the optical passband. In particular, we differentiate those 3D metallic PBG architectures that exhibit the required passband from those that do not, and we propose an optimum filament architecture.

We study metallic PCs with various structures, such as woodpiles [20], square spirals [8], slanted pore materials [21], and inverse opals [22]. We identify a unique electromagnetic dispersion relation in metallic, inverse diamond:3 square spiral [8] PBG filaments that may be ideal for incandescent lighting. In this architecture, a group of bands is isolated from the high frequency continuum, in the background of a huge band gap starting from zero frequency. When the filament consists of suitable air spirals in a background of iridium (Ir) metal and the lattice constant $a$ =400 nm, the isolated bands of the inverse spiral filament occur in a visible range centered near 670 nm. This occurs when the spiral structure parameters (see Ref. [8] for detailed definitions) are chosen as $[L,c,r]=[1.2a,1.7a,0.20a]$, where $L$ is the length of a single segment of each spiral arm, $c$ is the (vertical) lattice constant along the axis of the spiral, and $r$ is the radius of the (hollow) cylindrical spiral arms. In this case, the "elbows" of the square spiral arm coincide nearly with the third nearest neighbor points of a diamond lattice, in which the spiral axes point along the (1,0,0) direction of the diamond lattice. The frequencies of the isolated bands can be adjusted by varying the metallic bulk plasma frequency, $\omega_p$ (using different metals) and altering the lattice constant. A small lattice constant will cause a blueshift of the isolated bands. Similarly, a large lattice constant and higher $\omega_p$ will cause a redshift of the isolated bands.

Energy from electrical current in the PBG filament can be dissipated in at least three ways. Electronic scattering from phonons in the metal will contribute to the measured temperature of the filament. Electronic scattering from or near the exterior surface of the overall filament contributes to conventional forms of radiation into the featureless electromagnetic vacuum of free space. Electronic collision with the interior surfaces of the microstructured metallic filament may excite localized surface plasmon resonances [16] that emit light into the engineered electromagnetic vacuum, exclusively through the optical passbands of the PBG. In this interior, radiative decay channel, light emission at wavelengths, shorter and longer than the passband is suppressed. Energy that is dissipated into modes of frequency below the passband must either diffuse to the exterior filament surface to be radiated into the conventional light bulb spectrum or be up converted by a nonlinear process into the passband escape window. This energy enters the nonequilibrium distribution of photons in the passband and can likewise escape into free space through air channels that extend to the exterior surface of the filament. This leads to enhanced energy conversion efficiency into a desired band of optical frequencies and may have dramatic consequences for incandescent lighting. If, on the other hand, the PBG filament is placed within an isothermal enclosure, and the emitted photons are allowed to equilibrate with their interior sources, it is likely that this enhanced light emission, into a specified frequency band, will revert to that of a conventional filament [3,23].

The application of metallic PBG filaments to practical incandescent lighting requires careful investigation of the structural stability of such a microstructured filament under prolonged high temperature conditions. The large amount of interior surface area in the filament may require additional treatment of the filament to prevent degradation due to surface diffusion of metal atoms.

Room temperature applications of our spiral metallic filament architecture include optical sensing and enhanced photochemistry [24]. Both of these applications make use of the strong coupling of light to molecules passing through the interior void regions of the spiral filament. The synergy of plasmonic resonances and photonic crystal enhancement of the local electromagnetic density of states throughout the void channels of the filament provides intense and focused interior electromagnetic fields. Previously, strong coupling effects due to plasmonic resonances of metallic nanoparticles and nanoparticle dimers have been investigated [25–27] for improved photochemical reaction yield. In our metallic PBG filament, a large volume of strong coupling between optical fields and reacting molecules is possible. The void channels of our filament also enable natural guiding of molecular species to the required strong coupling regions.

This paper is organized as follows. In Sec. II, we calculate the band structure of various metallic photonic crystals (PCs), such as woodpiles [20], inverted opals [22], inverse square spirals [8], slanted pore materials [21], and holographic lithography defined PBG structures [28]. In Sec. III, the tungsten woodpile structure is considered in detail to compare with experimental observations of Lin *et al.* [5]. We demonstrate agreement of specific features of our theoretical calculations with the experiment. In Sec. IV, we describe the new contribution to light emission into engineered optical passbands from electrical pumping of the inverted square spiral filament backbone. Finally, a summary and discussion is presented in Sec. V.

## II. BAND STRUCTURE OF METALLIC PHOTONIC CRYSTALS

The band structures of metallic PCs are calculated by the FDTD method [29,30]. The dielectric constant of metal is described by the Drude model, $\varepsilon=1-\omega_p^2/(\omega^2+i\omega\omega_\tau)$, where $\omega_\tau$ is the damping frequency. This damping frequency may be regarded as the inverse of the electronic scattering time $\tau$ in the metal, giving rise to electrical resistance and associated with the temperature of the phonon bath in the metal. In the band structure calculations, we take $\omega_\tau=0$. Usually, $\omega_\tau$ is of the order about 1% of $\omega_p$ [31]. Ignoring the $\omega_\tau$ does not lead to a significant change of the real part of the dielectric constant $\varepsilon$ or change the band structure. This is verified in subsequent calculations of radiation, in which nonzero $\omega_\tau$ is used. However, $\omega_\tau$ does lead to absorption losses for interior electromagnetic modes.

We first consider the woodpile structure used in the experiment of Lin *et al.* [5]. Our band structure calculations reveal a large plasma screening gap in the long wavelength range due to the negative dielectric constant of tungsten below its bulk plasma frequency $\omega_p=9.74\times10^{15}$ s$^{-1}$, or to compare with the frequencies in Fig. 1(a), $a/\lambda_p=7.76$. No other photonic band gaps occur for the tungsten woodpile structure used in the experiment. This means that light emission from the interior surfaces is not funneled into a specific finite band of frequencies. However, enhanced light emission from the interior can take place in specific modes of the band structure above the *effective* plasma cutoff frequency of $a/\lambda=0.54$.
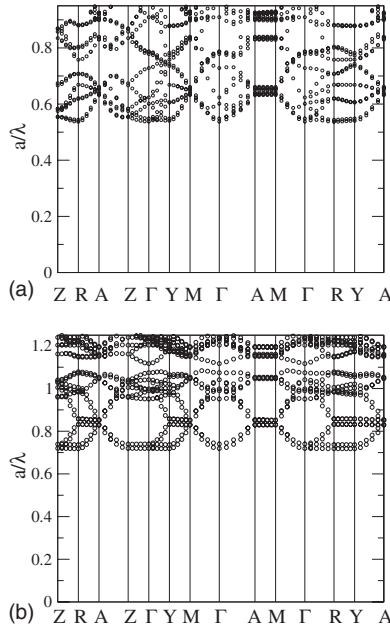
FIG. 1. The band structures of metallic woodpiles using $\varepsilon(\omega)$ $=1-(\omega_p/\omega)^2$. The lattice constant (a) is 1.5 $\mu$m and the height of the rod $(h)$ is 0.75 $\mu$m. (a) Tungsten woodpile with rod width 0.5 $\mu$m (similar to filaments fabricated by Lin *et al.* in Ref. [5]) has an effective plasma cutoff at $a/\lambda=0.54$, with no optical passbands below and no PBG above. The dimensionless plasma frequency of bulk tungsten $a/\lambda_p=7.76$ is used in our calculation. (b) Cu woodpile with rod width 0.9 $\mu$m. Here a small PBG centered at $a/\lambda$ $=1.10$ occurs above the effective plasma cutoff at $a/\lambda=0.72$. The dimensionless plasma frequency of bulk copper $a/\lambda_p=8.94$ is used in our calculation.

While the observation [5] of anomalous light emission is an indication of the importance of interior optical modes in a microstructured filament, the optimization of interior light emission is facilitated by an isolated optical passband. We have performed an extensive study of band structures, varying the structural and material parameters of various metallic woodpile filaments. For example, using copper, we find a narrow band gap above the effective plasma screening (fundamental) gap near $a/\lambda \approx 1.05$ gap in the short wavelength range. When the lattice constant $a=1.5$ $\mu$m, the rod height $h=0.75$ $\mu$m, and the rod width is 0.9 $\mu$m, the gap to midgap ratio of Cu (bulk plasma frequency $\omega_p=1.12\times10^{16}$ s$^{-1}$, or $a/\lambda_p=8.94$) woodpile structure is about 3%. The band structure is plotted in Fig. 1(b). This secondary PBG is too small to provide effective enhancement of light emission into a prescribed band. Our calculations suggest that the woodpile architecture, while capable of providing interesting anomalies in quasithermal light emission, is not optimal for wavelength emission-band selection in an incandescent PBG filament.

We have also studied a variety of inverse opal metallic filaments. Recently a tungsten-based inverse-opal structure was fabricated by von Freymann *et al.* [9]. We calculate the band structure of an idealized tungsten inverse opal (using Drude parameters $\omega_p=9.74\times10^{15}$ s$^{-1}$, $\omega_\tau=0$) in Fig. 2(a). The bands below the effective plasma cutoff frequency ($a/\lambda_p=0.83$) are extremely flat, with vanishing group veloc-
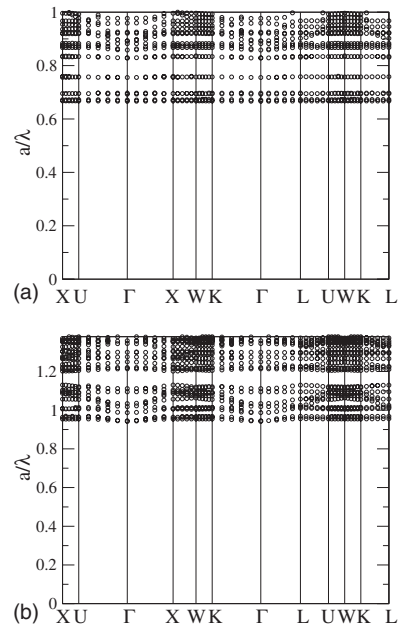


FIG. 2. Band structure of inverted opals made of various metals. The radius of spheres used to fabricate the opal is 315 nm and the coating thickness of metal is 40 nm. (a) Tungsten inverse opal. Bulk tungsten plasma frequency $\omega_p=9.74\times10^{15}$ s$^{-1}$ ($a/\lambda_p=4.61$) is used. (b) Silver inverse opal. Bulk silver plasma frequency $\omega_p$ $=1.37\times10^{16}$ s$^{-1}$ ($a/\lambda_p=6.48$) is used.

ity. These modes are localized and cannot propagate inside the structure. A much higher plasma frequency $\omega_p=1.37$ $\times10^{16}$ s$^{-1}$ (or $a/\lambda_p=6.48$) can be obtained using silver (Ag) instead of tungsten. When the coating of silver is thick enough, there is a small gap above the fundamental gap. We depict the band structure of a silver inverted opal in Fig. 2(b). The gap to midgap ratio is about 6%. The bands in the inverse opal filaments appear to be very flat surface plasmon modes rather than air-guided modes in the pores of the microstructure.

Of all the structures we have studied, a certain class of inverse square spiral structures [8] has the largest secondary PBG. Equivalently, this can be described as an isolated optical passband below the effective plasma screening gap (see Fig. 3). When the parameters $[L,c,r]=[1.2a,1.7a,0.2a]$ [8], the gap to midgap ratio of this secondary PBG is the largest, about 22.7%. Roughly speaking these structure parameters correspond to connecting the third-nearest-neighbor points of a diamond lattice and this architecture is referred to as "inverse diamond:3" [8]. For an iridium (Ir) inverse spiral filament, the corresponding band structure is shown in Fig. 3(b). The bulk plasma frequency of Ir is taken as 7.8 eV [32] and the melting temperature of Ir is 2446 °C [33]. Within the Drude model we use $\omega_p=1.18\times10^{16}$ s$^{-1}$, $\omega_\tau=0$. Clearly, if the structure is electrically pumped, radiation from the interior surfaces (at frequencies below $a/\lambda=0.75$) will be emitted exclusively into the engineered optical passband.

The high melting point and high plasma frequency of iridium make it promising for electrically pumped, visible light emission. Recently, important milestones have been demonstrated in the accurate fabrication of iridium-based structures using atomic layer deposition (ALD) [34]. Similar ap-
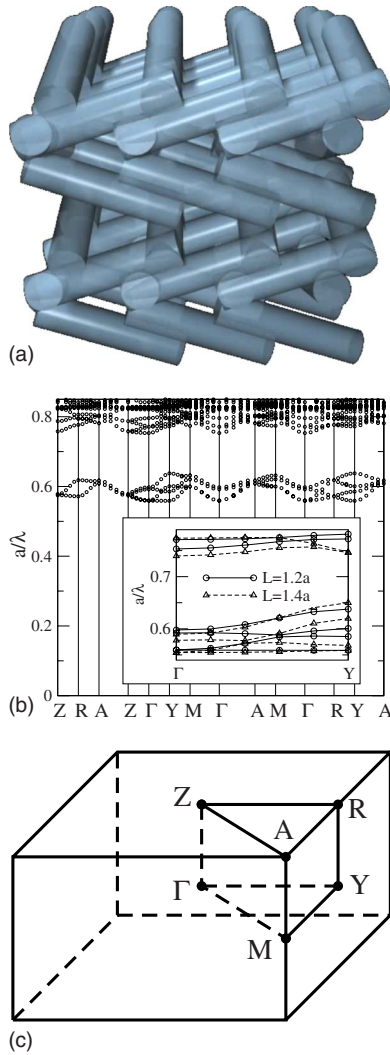
(a)



(b)



(c)

FIG. 3. (a) (Color online) Image of square spiral structure prior to inversion. (b) The band structure of the iridium inverse square spiral using the Drude model with plasma frequency $\omega_p = 1.18 \times 10^{16} \text{ s}^{-1}$ and damping rate $\omega_\tau = 0$. The lattice constant is 400 nm. The square spiral parameters are $[L,c,r] = [1.2a, 1.7a, 0.22a]$. The inset is the lowest six bands for the $[L,c,r] = [1.2a, 1.7a, 0.22a]$ and $[L,c,r] = [1.4a, 1.7a, 0.22a]$ square spirals. (c) Brillouin zone depicting high symmetry points in **k** space. A rectangular prism of dimensions $a \times a \times c$ is used as the (real space) unit cell. The coordinates of these points are $\Gamma$ (0,0,0), $Z$ $(0,0,\pi/c)$, $R$ $(0,\pi/a,\pi/c)$, $A$ $(\pi/a,\pi/a,\pi/c)$, $Y$ $(0,\pi/a,0)$, and $M$ $(\pi/a,\pi/a,0)$.

proaches can be used to infiltrate iridium into the interior void regions of a template spiral PC consisting of solid SiO2 spiral posts. After infiltration the SiO2 posts can be removed by selective etching, leaving behind the desired iridium-based inverse diamond:3 architecture. Metallic nanoparticles can also be embedded on the interior surfaces of the metallic PC by the reduction of metal nanowires, suitably infiltrated into the void network of the PC [35]. These nanoparticles may emit light into the isolated optical passband of the iridium photonic-band-gap filament.

The robustness of the gap between the isolated bands and the continuum is estimated by varying the structural parameters in the photonic band structure calculation. As shown in
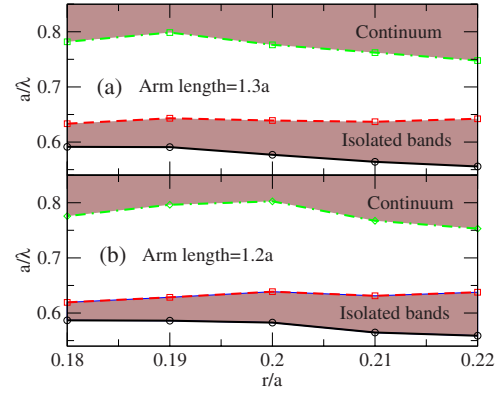


FIG. 4. (Color online) Frequencies of plasma screening gap, the optical passband (isolated bands), and the secondary PBG of iridium inverse square spiral as a function of arm radius. Here, $\omega_p = 1.18 \times 10^{16} \text{ s}^{-1}$ and $\omega_\tau = 0$. The lattice constant is $a = 400$ nm. (a) Arm length $1.3a$. (b) Arm length $1.2a$.

Fig. 4, the gap to midgap ratio for the secondary PBG remains larger than 15% for a broad range of parameters (rod diameter is varied between 144 and 176 nm, and the arm length is varied between 480 and 520 nm). This suggests that the engineered optical passband (and its separation from the continuum) is rather robust to disorder in the inverse diamond:3 architecture. This robust, isolated, optical passband (with bandwidth suitable for broadband lighting applications) appears to be unique to the inverse diamond:3 architecture. Such a passband does not occur in the inverse diamond:1 architecture (where shorter spiral arms connect the first nearest-neighbor points of diamond) or in the inverse diamond:5 architecture (where longer spiral arms connect the fifth nearest-neighbor points of diamond), as discussed below.

In order to understand the emission and propagation of light within the interior of the PBG inverse spiral filament, it is instructive to consider the electromagnetic mode profile within the passband. Electric fields are often large near the sharp edges of metals. This is apparent in our inverse diamond:3 spiral filament. The electric and magnetic field inside the hollow-metallic arms of the spirals are plotted in Fig. 5, revealing electric field concentration in the air region near sharp edges or corners of the metallic enclosure, where spiral arms either terminate or join with neighboring spiral arms. Here, we use the $[L,c,r] = [1.2a, 1.7a, 0.22a]$ square spiral (the same parameters as those in Fig. 3) to study the electric field pattern. The inverse square spiral structure has two kinds of sharp edges, leading to two kinds of bands, one within the optical passband range and the other near the top of the secondary PBG. The structure consists of cylindrical arms stacking on each other (with a shift along the $x$ or $y$ axis). The first pair of metallic knife edges is formed by overlap of the side walls of arms stacking on top of each other. In Fig. 6(a), these long straight knife edges are highlighted. These metallic knife edges occur along the side wall of a periodic array of metallic boxes with a figure-eight cross section. The regions of the spiral arms that do not overlap other spiral arms correspond to narrow passageways in which light can leak from one metallic box to a neighboring
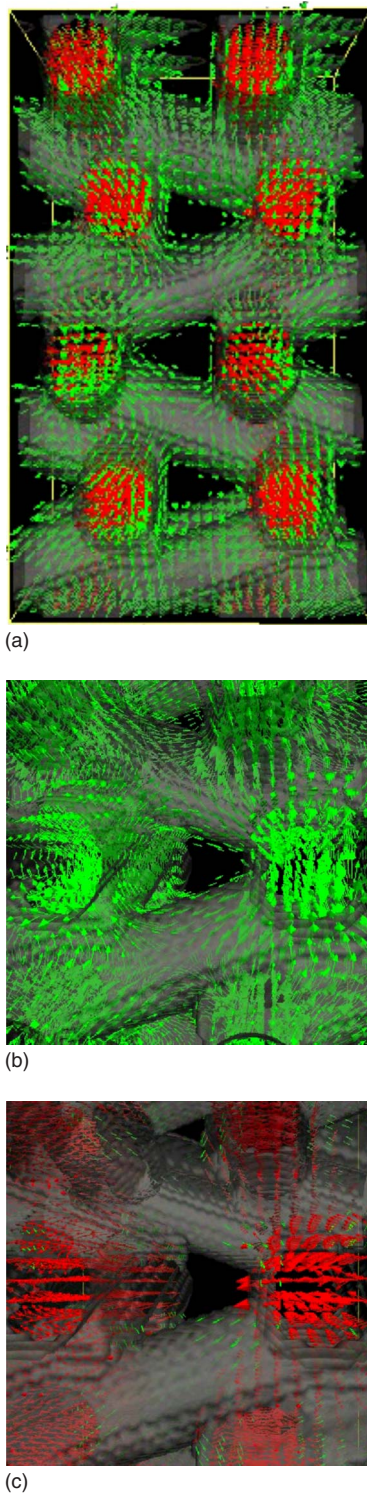
(a)

(b)

(c)

FIG. 5. (Color online) The electric field (red arrow) and magnetic field (green arrow) in the inverted spiral structure. (a) Electric and magnetic fields, within the optical passband of an iridium-based inverse square spiral with parameters given by Fig. 3, obtained by FDTD are shown propagating through the connected interior void network of filament. (b) Close-up shows magnetic field circulating around loops within the air-void network. (c) The passband mode is characterized by a very strong electric field concentrated near the sharp-edge grill structure [see Fig. 6(a)] of the void network where two hollow metallic cylinders overlap.
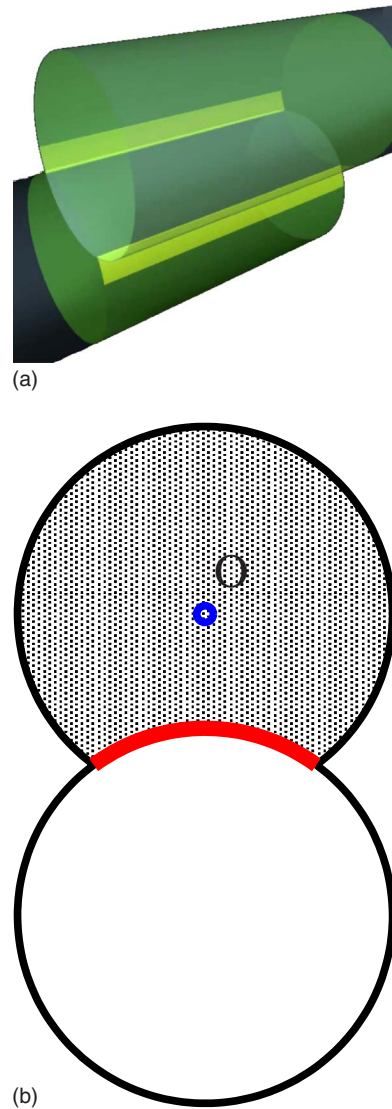


(a)

(b)

FIG. 6. (Color online) The interior void regions of the inverse diamond:3 spiral metallic filament form a lattice of hollow-metallic "boxes" supporting electromagnetic modes of two types. In the first type (a) electric field amplitude is highly concentrated near the tips of V-shaped grill structures on either side of each metallic box. These modes comprise the optical passband within the effective plasma gap of the structured filament and may provide strong light emission into the isolated band. In the second type (b), electric field amplitude is highest near the intersection of one arm elbow with another arm. These modes comprise the photonic band edge modes at the top of the secondary PBG (just above the isolated optical passband). The shaded area is the bottom of one arm (interface of metal and air). Part of the circle is chopped off by the overlapping arm. The highlighted (thick line) red arc is the edge formed by overlapping arms. The blue point $O$ in the middle of shaded area is where dipoles are placed in the latter part of this paper to calculate emissions.

metallic box. Electromagnetic modes within the isolated optical passband have very large electric field amplitudes near the pair of knife edges within each metallic box. Surface plasma resonances localized near these edges will exhibit very strong coupling to the optical passband modes.

The lower edge of the secondary PBG opens at $k = (0, \pi/a, 0)$ [$Y$ point in Fig. 3(b)]. According to Bloch theorem, the electric field of this mode has opposite signs at the nearby metal boxes. Since knife edges in our metallic boxes are almost parallel to the $x$ ($y$) axis, longer spiral arms lead to longer overlap and shorter distance between two nearby metal boxes. Therefore, the fields of opposite signs are close to each other when the arm length increases, causing the passband to rise in frequency. When the radius of the arms increases, the sharp knife edges within a given metallic box gradually disappear. This decreases the field localization near the sharp edges, leading to a broadening of the isolated bands. Increasingly, long spiral arms or large arm radius will eventually cause collapse of the secondary PBG that separates the optical passband and the continuum [see the inset of Fig. 3(b) for the dependence on $L$]. As a result, the inverse diamond:5 architecture [8] (with spiral arms connecting fifth nearest-neighbor points of the diamond lattice) is not suitable for strongly channeled quasithermal light emission over a finite band of frequencies. On the other hand, structures with short spiral arms or small radius arms lack sufficient overlap between nearby arms. In this case, the required metallic boxes are either too small or unable to form at all. Consequently, isolated optical passbands do not form. The inverse diamond:1 architecture (with spiral arms connecting nearest-neighbor points of the diamond lattice) is, therefore, not suitable for engineered light emission from the interior surfaces of the metal filament. Only spiral structures with arms around $L = 1.2a$ and rods around $r = 0.2a$ enable engineering of isolated optical passbands.

Another type of edge in the metallic box is formed by the elbow of an arm (end face of the cylinder) overlapping the hollow region of a nearby spiral arm. This leads to oval-shaped end faces (more precisely the intersection set of two circular arm cross sections) of the metallic boxes. The edge is highlighted red in Fig. 6(b). These metallic end faces also act as high field amplitude source regions for another set of optical modes that propagate through the interior of the PBG filament. The bands, associated with these end faces, occur at the lower edge of the optical mode continuum just above the secondary PBG and the effective plasma cutoff. A larger rod radius will elongate the end face, leading to deconfinement (less localization) of the electric field, i.e., lowering the band. A longer arm will further separate the end faces of the metallic box at $z = 1/4c$ and $z = 3/4c$, again deconfining the electromagnetic mode and lowering the band. When $\mathbf{k} = (0, \pi/a, 0)$, where the electric fields at $z = 1/4c$ and $z = 3/4c$ have opposite signs, the continuum edge is lowered further. As a result, the secondary PBG closes at this point.

We have studied in detail the band structures of a variety of other 3D PBG architectures including metallic slanted pore [21] filaments, metallic filaments defined by optical interference lithography [28], and optical phase mask lithography [36]. Throughout the entire range of structural and material parameters studied, we were unable to find an isolated optical passband in these alternative architectures. This underscores the uniqueness of the inverse diamond:3 square spiral, metallic "box and grill," filament.

## III. COMPARISON WITH EXPERIMENTS

In order to compare with previous experiment results of Lin *et al.* [5], we briefly review them here. When the tungsten woodpile filament is driven by an electrical current and the lattice temperature is measured to be 1190 K, quasithermal light emission consists of a small peak at $\lambda \approx 2.5$ $\mu$m and a strong peak at $\lambda \approx 1.8$ $\mu$m. At a higher lattice temperature of 1535 K, the stronger peak dominates the spectrum and shifts to $\lambda \approx 1.5$ $\mu$m [5].

As temperature increases, $\omega_p$ changes little, but $\omega_\tau$ increases significantly. In the Drude model [31], the conductivity $\sigma$ is related to $\omega_p$ and $\omega_\tau$ by $\sigma = \omega_p^2/(4\pi\omega_\tau)$, where $\sigma$ has units of cm$^{-1}$. This can be expressed in terms of the dc resistivity $\rho_0$ as follows:

$$\sigma(\text{cm}^{-1}) = \frac{1}{2\pi c[\rho_0(\text{s})]} = \frac{9 \times 10^{11}}{2\pi c[\rho_0(\Omega \text{ cm})]},$$

where $\rho_0$ is in units of $\Omega$ cm and $c$ is the speed of light. Therefore, $\omega_\tau$ is proportional to the dc resistivity, $\omega_\tau = \omega_p^2 c \rho_0/(1.8 \times 10^{12})$.

We use the temperature dependence of the dc resistivity $\rho(T)$ to estimate the temperature dependence of $\omega_\tau$. We define a reduced resistivity $r(T) \equiv \rho(T)/\rho_0$, where $\rho_0$ is the resistivity at 0 °C. In the Bloch-Gruneisen model [37], the reduced resistivity is a function of the reduced temperature $T/\theta$: $r_T = 1.056(T/\theta)F(\theta/T)$. The value of characteristic temperature $\theta$ (usually associated with the high frequency Debye cutoff of the phonon spectrum in the metal) and function $F(\theta/T)$ for various metals can be found in Ref. [37]. In conventional bulk metals, the temperature $T$ that appears in the expression for resistivity is the same as the measured lattice (phonon) temperature. In our model, the system temperature is defined through the electrical resistivity rather than the lattice vibrational temperature. It would be of considerable interest to measure the true resistivity vs lattice temperature in the structured metal, where we expect other important contributions to resistance apart from phonon scattering.

We consider the same tungsten woodpile structure used in the experiment by Lin *et al.* [5]. In our calculation, the bulk plasma frequency $\omega_p$ is chosen to be $5.17 \times 10^2$ cm$^{-1}$ ($9.74 \times 10^{15}$ s$^{-1}$) [31]. In dimensionless frequency, $a/\lambda_p = 7.76$, where the lattice constant $a = 1.5$ $\mu$m. The damping frequency $\omega_\tau = 4.99 \times 10^{14}$ s$^{-1}$ [31]. The corresponding band structure is depicted in Fig. 1(a). There is a huge band gap for $\lambda > 2.8$ $\mu$m. This represents the effective plasma screening gap for the microstructured metal, which occurs at frequencies well below the bulk plasma frequency of tungsten metal. The bandgap suppresses the radiation in the long wavelength range from the interior surfaces of the woodpile structure, while enabling a rapid onset of light emission from interior modes for wavelength $\lambda < 2.8$ $\mu$m. This interior light emission spectrum is superimposed on the conventional emission spectrum from the exterior surface of the woodpile filament. This behavior is consistent with experimentally observed spectrum. However, no band gap is found for $\lambda < 2.8$ $\mu$m, making it impossible to efficiently suppress interior radiation in the near infrared wavelength range.

We now simulate the electromagnetic emission pattern from sources placed at various locations within a finite size woodpile structure. We consider a finite tungsten woodpile filament placed in vacuum. In our FDTD simulations, the open boundary is represented by an (perfectly matched layer [29,38]) absorbing surface surrounding all the exterior surfaces of the filament. In this simulation, all radiation from the filament escapes into free space. There is no feedback from the escaped radiation field to the filament and thermodynamic equilibrium cannot be established between the emitted photons and the dipole radiators within the filament. Due to the discretization scheme of coordinate space, each dipole radiator is either in the air or in the metal. We place dipoles in the air near the interior metal surfaces. The orientations of dipoles are chosen normal to the metal surfaces because the electric field is almost normal to the metal surface (H polarization). Since metals (such as tungsten and iridium) are good conductors at optical frequencies, electric fields tend to be normal to the surface of these metals, and dipoles parallel to the metal surface are difficult to couple to the electric field. H-polarized light emission of this type, is consistent with radiation from localized surface plasmon resonances that may be excited through electrical pumping of the metallic backbone. The overall radiation spectrum is obtained by integrating the Poynting vector over a closed surface about 2/3 lattice constant away from the structure. Further increasing the distance between the structure and the closed surface does not lead to discernible changes in the simulated radiation spectrum.

A finite structure of $5 \times 5 \times 2$ unit cells is used to calculate the radiation from a dipole, which is placed in the middle of various side walls of the rods, with orientation normal to the surface. The dipole oscillates over a range of different frequencies with amplitudes that we assume are related to the underlying lattice vibrational temperature $T$. This is the same temperature we assume determines the electrical resistivity of the filament due to electron-phonon scattering. In this simulation, we ignore possible contributions due to nonequilibrium (ballistic) electrons that may excite dipole resonators directly on higher energy scales than the thermal background. However, the emitted radiation is not in the thermal equilibrium with the filament (as a result of the open boundary condition) and we refer to this as "quasithermal" radiation. In Fig. 7, this quasithermal radiation shows a strong suppression for $\lambda > 2.5$ $\mu$m except when the dipole is placed on the first woodpile layer near the exterior surface of the filament. As the lattice vibrational temperature increases, the radiation from the exterior surface layer changes only slightly. However, the radiation from the interior layers decreases more rapidly due to the increase in electrical resistance and concomitant electromagnetic absorption described by $\omega_\tau$. For the woodpile structure, with no isolated optical passband through void regions of the crystal, the exterior surface emission plays an important role at high temperature.

To estimate the quasithermal (nonequilibrium) radiation from the tungsten woodpile, the radiation from each layer is summed, and multiplied by the Boltzmann coefficient $\hbar\omega/[\exp(\hbar\omega/kT) - 1]$ as follows: we integrate the Poynting vectors over a surface that encloses the finite size filament using an interior dipole emitter of fixed amplitude. As the
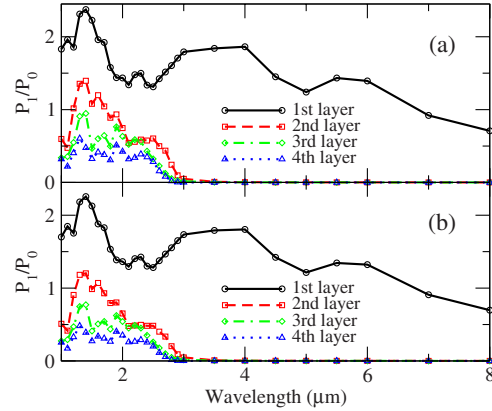


FIG. 7. (Color online) The radiation ($P_1$), through all surfaces, from a dipole inside the tungsten woodpile structure, occupying the volume $0 < x < 5a$, $0 < y < 5a$, and $0 < z < 4a$. $P_0$ is the radiation of a dipole in the free space. The distance from these dipoles to the surface are $0.5h$ (first layer), $1.5h$ (second layer), $2.5h$ (third layer), and $3.5h$ (fourth layer), respectively. The dipoles are placed at positions $(2.5, 2.5, 0.25)a$ in the first layer, $(2.5, 2.5, 0.75)a$ in the second layer, $(2.5, 2.35, 1.25)a$ in the third layer, and $(2.35, 2.5, 1.75)a$ in the fourth layer. (a) $T=1200$ K. (b) $T=1500$ K.

frequency of the dipole emitter is varied, its oscillation amplitude is kept fixed. However, we mimic the effect of thermal excitation of the dipole by multiplying the overall output energy from the filament by the Boltzmann weight factor. As shown in Fig. 8, quasithermal radiation from the finite structure is not completely suppressed for $\lambda > 3$ $\mu$m, due to the exterior surface emission (see Fig. 7). In Fig. 8, the blackbody spectral profile (not on the same scale as the FDTD results), is plotted for comparison with the spectral profile from the PBG filament. In the experiment of Lin *et al.* [5], when the lattice vibrational temperature is measured to be about 1500 K, the radiation from the woodpile photonic crystal is about five times that of an ideal blackbody at $\lambda \approx 1.5$ $\mu$m, at the same temperature. Lin *et al.* suggest that the emission from tungsten photonic crystal can exceed that of an ideal blackbody emitter because the tungsten photonic crystal is not in a thermal equilibrium state [15]. Indeed there are at least four modes of energy that we associate with the microstructured filament: (i) electrons in the driving current,
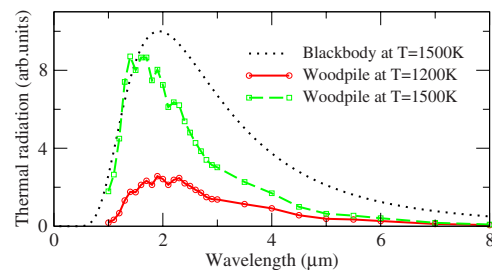


FIG. 8. (Color online) Estimation of the quasithermal (nonequilibrium) radiation from the tungsten woodpile. Energy emitted by dipoles, over a broad range of frequencies at fixed oscillation amplitude, in each layer (in Fig. 7) is summed and multiplied by the Boltzmann coefficient $\hbar\omega/[\exp(\hbar\omega/kT) - 1]$ to obtain the estimation.

(ii) surface dipole resonators, (iii) lattice vibrations of metal atoms, and (iv) photons emitted by the filament. Under normal operation of a light-emitting filament in free space, these subsystems may not be in equilibrium with each other.

In our calculation, quasithermal radiation from the filament decreases when $\lambda > 2.5$ $\mu$m, in agreement with experimental results and the band structure calculations. At a phonon temperature of $T = 1500$ K, radiation from the PBG filament is more concentrated between $\lambda = 1.5 \sim 2.0$ $\mu$m than in the ideal blackbody. This tendency agrees with the experiments. Our simulations cannot produce sharp peaks around 1.8 and 1.5 $\mu$m because we only place the dipole emitters in four positions in our calculations. Unlike the analysis of nonlinear Bloch waves in a 2D PBG filament considered recently [17], our simulation does not take into account the direct nonlinear response of dipole resonators on the interior surface of the filament to nonthermal excitation by a driving current. Also quasithermal radiation emanates from all parts of the filament, a simulation of which is beyond our computational ability. Nevertheless, our calculations capture important qualitative features of the experiment. This provides further plausibility to our simulation results, presented below, on the optimized inverse square-spiral filament.

## IV. SPECTRAL PROFILE FOR QUASITHERMAL LIGHT EMISSION FROM INVERSE SPIRAL PBG FILAMENT

In this section, we use the same method described in the previous section to simulate the approximate spectral emission profile from an inverse square spiral filament consisting of iridium. Here, a finite structure of $3 \times 5 \times 3$ unit cells ($3a \times 5a \times 5.1a$) is used to calculate the radiation from dipoles inside the structure. All dipoles are at the centers of the circular faces of the arm's ends [point $O$ in Fig. 6(b)]. The directions of these dipoles are normal to the metal surface. The damping frequency is estimated from the dc conductivity ($\sigma_0$) using $\sigma_0 = \omega_p^2/(4\pi\omega_\tau)$ [31]. At temperature $T = 1500$ K, we use $\omega_p = 1.18 \times 10^{16}$ s$^{-1}$ and $\omega_\tau = 3.56 \times 10^{14}$ s$^{-1}$ in our calculations.

The overall radiation through the closed surface (normalized to the power emitted in the vacuum) is plotted in Fig. 9. The ratio here does not indicate whether the PBG filament can emit more radiation than a blackbody. It has been shown [17] for a simple 2D metallic PBG filament, supporting nonlinear surface resonances, that very high output power with laserlike input-output characteristics is possible within a passband, provided that the filament is driven out of equilibrium by the pumping process. This phenomenon is beyond the scope of our present calculation. Nevertheless, the pronounced peaks around 670 nm show that the inverse spiral structure can successfully suppress the thermal radiation for both the long and short wavelength range. This suggests that an architecture with an isolated optical passband is more suitable to modify thermal emission than previously studied woodpile structures.

Due to the surface effect, the peak emission from a dipole placed in the third layer (it is closer to the surface than the first layer) has a small red shift. The radiation from the di-
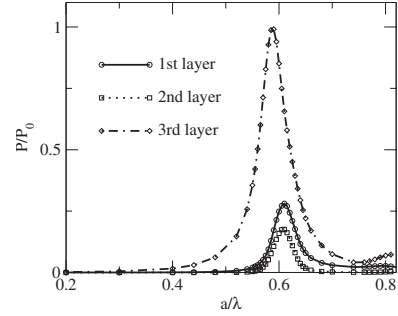


FIG. 9. The quasithermal power (as defined in Fig. 8 emitted, through all the surfaces, from dipoles inside the square spiral structure, occupying the volume $0 < x < 3a$, $0 < y < 5a$, and $0 < z < 5.1a$, at $T = 1500$ K. The bulk plasma frequency $\omega_p = 1.18 \times 10^{16}$ s$^{-1}$ and damping frequency $\omega_\tau = 3.56 \times 10^{14}$ s$^{-1}$ are used in our calculations. $P_0$ is the corresponding power emission in ordinary vacuum. The dipoles are in the $y$ direction, normal to the surface of the metal matrix. The emitting dipoles are placed at positions $(0.7, 2.9, 2.65)a$ in the first layer, $(1.7, 2.9, 2.65)a$ in the second layer, and $(2.7, 2.9, 2.65)a$ in the third layer. Since there are only three layers in the $x$ direction, the dipole in the third layer is actually closer to the surface ($x = 3a$) than the one in the first layer is.

pole near the surface is larger than those from the inner structure because of the absorption of the metal, indicating that the radiation near the surface plays an important role, especially at high temperature. However, if the system is driven out of equilibrium by a nonthermal pumping mechanism, surface resonances may provide gain to the optical passband modes and overcome resistive losses in the hot metal [17].

## V. CONCLUSION

To conclude, we have found an electromagnetic passband in metallic inverse square spirals, which is suitable for selective quasithermal radiation and incandescent lighting. A group of bands is isolated from the continuum and resides within the otherwise forbidden plasma gap of the structured metallic filament. Radiation from the interior of the filament into unwanted long and short wavelength ranges is suppressed, leading to efficient band-selective quasithermal emission. These metallic PBG structures can be used as filaments of light bulbs to emit visible light. They may also be useful in thermophotovoltaics [39] to absorb broadband radiation, channel it into a specific emission band, and then generate electric power in a photovoltaic device that is most receptive to light within that band. At high temperatures, thermal radiation near the surface plays an important role. Our calculations are consistent with recent experimental studies [5,15] of tungsten woodpile filaments, but indicate that the inverse spiral filament may provide considerable enhancement of the desired band-selective light emission characteristics.

It is particularly important to address the issues of thermodynamic equilibrium and deviations from equilibrium between light emitters within the filament and the surrounding

radiation field. This requires closed or partially closed boundary conditions (reflecting walls) surrounding the light emitting filament and solution of the coupled equations of motion of the dipole resonators and the surrounding radiation field. This is problematic for finite-difference time-domain simulation since any small reflecting enclosure modifies the electromagnetic density of states, surrounding the filament, from that of free space. On the other hand, a very large computational domain (with a density of states closes to that of free space) requires prohibitive amounts of computational memory. It is also of considerable importance to understand the nature of excitation of surface resonances within structured metal through electrical pumping of the filament. For practical application of PBG metallic filaments, an important issue is the stability of the material under prolonged heating and temperature cycling. The large interior surface area of the filament enables surface diffusion of metal atoms that may alter the structure of the filament in the course of time. These issues need to be studied and addressed. We hope that our analysis of metallic PBG architectures will stimulate further materials science and experimental studies of more optimal structures for incandescent lighting.

[1] M. Planck, *The Theory of Heat Radiation* (Dover, New York, 1959).

[2] G. Kirchhoff, Monats. Akad. Wiss. Berlin 783 (1859) (presented Dec. 11, 1959); Ann. Phys. **109**, 275 (1860).

[3] P. M. Robitaille, IEEE Trans. Plasma Sci. **31**, 1263 (2003).

[4] I. El-Kady, W. W. Chow, and J. G. Fleming, Phys. Rev. B **72**, 195110 (2005).

[5] S. Y. Lin, J. Moreno, and J. G. Fleming, Appl. Phys. Lett. **83**, 380 (2003).

[6] S. John, Phys. Rev. Lett. **53**, 2169 (1984); **58**, 2486 (1987).

[7] E. Yablonovitch, Phys. Rev. Lett. **58**, 2059 (1987).

[8] O. Toader and S. John, Science **292**, 1133 (2001); O. Toader and S. John, Phys. Rev. E **66**, 016610 (2002).

[9] G. von Freymann, S. John, M. Schulz-Dobrick, E. Vekris, N. Tétreault, S. Wong, V. Kitaev, and G. A. Ozin, Appl. Phys. Lett. **84**, 224 (2004).

[10] J. G. Fleming, S. Y. Lin, I. El-Kady, R. Biswas, and K. M. Ho, Nature (London) **417**, 52 (2002).

[11] S. R. Kennedy, M. J. Brett, O. Toader, and S. John, Nano Lett. **2**, 59 (2002); S. R. Kennedy, M. J. Brett, H. Miguez, O. Toader, and S. John, Photonics Nanostruct. Fundam. Appl. **1**, 37 (2003).

[12] D. X. Ye, Z. P. Yang, A. S. P. Chang, J. Bur, S. Y. Lin, T. M. Lu, R. Z. Wang, and S. John, J. Phys. D: Appl. Phys. **40**, 2646 (2007).

[13] K. K. Seet, V. Mizeikis, S. Matsuo, S. Juodkazis, and H. Misawa, Adv. Mater. (Weinheim, Ger.) **17**, 514 (2005).

[14] T. Trupke, P. Würfel, and M. A. Green, Appl. Phys. Lett. **84**, 1997 (2004).

[15] S. Y. Lin, J. Moreno, and J. G. Fleming, Appl. Phys. Lett. **84**, 1999 (2004).

[16] A. Kubo, N. Pontius, and H. Petek, Nano Lett. **7**, 470 (2007); A. Kubo, K. Onda, H. Petek, Z. Sun, Y. S. Jung, and H. K. Kim, *ibid.* **5**, 1123 (2005).

[17] A. Kaso and S. John, Phys. Rev. A **76**, 053838 (2007).

[18] T. W. Ebbesen, H. J. Lezec, H. F. Ghaemi, T. Thio, and P. A. Wolff, Nature (London) **391**, 667 (1998).

[19] A. Kaso and S. John, Phys. Rev. E **74**, 046611 (2006).

[20] K. M. Ho, C. T. Chan, C. M. Soukoulis, R. Biswas, and M. Sigalas, Solid State Commun. **89**, 413 (1994).

[21] O. Toader, M. Berciu, and S. John, Phys. Rev. Lett. **90**, 233901 (2003).

[22] A. Blanco, E. Chomski, S. Grabtchak, M. Ibisate, S. John, S. W. Leonard, C. Lopez, F. Meswguer, H. Miguez, J. P. Mondia, G. A. Ozin, O. Toader, and H. M. van Driel, Nature (London) **405**, 437, (2000).

[23] C. Luo, A. Narayanaswamy, G. Chen, and J. D. Joannopoulos, Phys. Rev. Lett. **93**, 213905 (2004).

[24] H. Misawa (private communication).

[25] K. Kamada, Y. Tanamura, K. Ueno, K. Ohta, and H. Misawa, J. Phys. Chem. C **111**, 11193 (2007).

[26] K. Ueno, S. Juodkazis, V. Mizeikis, K. Sasaki, and H. Misawa, Adv. Mater. (Weinheim, Ger.) **20**, 26 (2008).

[27] K. Ueno, S. Juodkazis, T. Shibuya, Y. Yokota, V. Mizeikis, K. Sasaki, and H. Misawa, J. Am. Chem. Soc. **130**, 6928 (2008).

[28] O. Toader, T. Y. M. Chan, and S. John, Phys. Rev. Lett. **92**, 043905 (2004).

[29] A. Taflove and S. C. Hagness, *Computational Electrodynamics: The Finite-Difference Time-Domain Method*, 2nd ed. (Artech House, Boston, 2000).

[30] K. Sakoda, N. Kawai, T. Ito, A. Chutinan, S. Noda, T. Mitsuyu, and K. Hirao, Phys. Rev. B **64**, 045116 (2001); T. Ito and K. Sakoda, *ibid.* **64**, 045117 (2001).

[31] M. A. Ordal, R. J. Bell, R. W. Alexander, Jr., L. L. Long, and M. R. Querry, Appl. Opt. **24**, 4493 (1985).

[32] J. H. Weaver, C. G. Olsen, and D. W. Lynch, Phys. Rev. B **15**, 4115 (1977).

[33] *Thermal and Physical Properties of Pure Metals* edited by David R. Lide, CRC Handbook of Chemistry and Physics, 88th ed. (Internet version 2008) (CRC Press/Taylor and Francis, Boca Raton, FL, 2008).

[34] T. Aaltonen, M. Ritala, V. Sammelselg, and M. Leskelä, J. Electrochem. Soc. **151**, G489 (2004); K. Jefimovs, J. Vila-Comamala, T. Pilvi, J. Raabe, M. Ritala, and C. David, Phys. Rev. Lett. **99**, 264801 (2007).

[35] M. Knez (private communication); for a review see M. Knez, Material Matters **3**, 28 (2008).

[36] T. Y. M. Chan, O. Toader, and S. John, Phys. Rev. E **73**, 046610 (2006).

[37] *Handbook of Physical Quantities*, edited by I. S. Grigoriev and E. Z. Meilikhov (CRC Press, New York, 1997).

[38] S. D. Gedney, IEEE Trans. Antennas Propag. **44**, 1630 (1996).

[39] T. J. Coutts and M. C. Fitzgerald, Sci. Am. **7**, 90 (1998); M. Zenker, A. Heinzel, G. Stollwerck, J. Ferber, and J. Luther, IEEE Trans. Electron Devices **48**, 367 (2001).